

Recovering cores and cusps in dark matter haloes using mock velocity field observations

Rachel Kuzio de Naray^{1*†} and Tobias Kaufmann^{2‡}

¹ *Center for Cosmology, Department of Physics and Astronomy, University of California, Irvine, CA 92697-4575*

² *Institute of Astronomy, ETH Zürich-Hönggerberg, CH-8093 Zürich, Switzerland*

10 March 2011

ABSTRACT

We present mock DensePak Integral Field Unit (IFU) velocity fields, rotation curves, and halo fits for disc galaxies formed in spherical and triaxial cuspy dark matter haloes, and spherical cored dark matter haloes. The simulated galaxies are “observed” under a variety of realistic conditions to determine how well the underlying dark matter halo can be recovered and to test the hypothesis that cuspy haloes can be mistaken for cored haloes. We find that the appearance of the velocity field is distinctly different depending on the underlying halo type. We also find that we can successfully recover the parameters of the underlying dark matter halo. Cuspy haloes appear cuspy in the data and cored haloes appear cored. Our results suggest that the cores observed using high-resolution velocity fields in real dark matter-dominated galaxies are genuine and cannot be ascribed to systematic errors, halo triaxiality, or non-circular motions.

Key words: dark matter — galaxies: kinematics and dynamics — formation — hydrodynamics — methods: numerical — methods: N-body simulations.

1 INTRODUCTION

Cold Dark Matter (CDM) is one of the main constituents of the current standard model in cosmology, Λ CDM. N-body simulations based on the CDM paradigm predict dark matter haloes best-described by a steep (“cuspy”, “NFW”) power law mass density distribution (e.g. Navarro et al. 1996a). While the exact slope of the inner density distribution remains under debate (e.g. Moore et al. 1999; Graham et al. 2006; Stadel et al. 2009; Navarro et al. 2010), simulations all agree on producing a cuspy profile with a slope of $\alpha \sim -1$ in the central part of the halo (see the review of de Blok 2010).

Observed rotation curves of galaxies typically need a massive dark matter halo with a nearly constant density core in order to describe the data well. Ideal objects for observationally studying the “cusp-core problem” are low surface brightness (LSB) galaxies which are late-type, gas-rich, dark matter-dominated disc galaxies. Observations using long-slit spectra in $H\alpha$ (e.g. de Blok & Bosma 2002) or high-resolution two-dimensional velocity fields (Kuzio de Naray et al. 2006, 2008, hereafter K06 and K08,

respectively) show that a cored dark matter distribution (described e.g. by an pseudoisothermal sphere profile) provide a better fit to the data than a cuspy NFW dark matter profile. In the few cases where NFW models do reasonably fit the rotation curve data, the predicted values for concentrations c_{200} are very low and the circular velocity V_{200} at the virial radius very high, inconsistent with the cosmological (c_{200}, V_{200}) – relation, (see the review of de Blok 2010).

Most observational problems such as pointing errors, centering offsets and non-circular motions are likely too small to cause cusps to be mistaken for cores in the observations (de Blok 2010), but halo triaxiality has been claimed to explain the presence of cores. The simulation works of Hayashi et al. (2007) and Bailin et al. (2007), for example, showed that due to systematic non-circular motions introduced by a triaxial halo, cusps could be interpreted for cores if long-slit rotation curves were used. Similarly, bars inducing non-circular motions combined with projection effects can create the illusion of a constant-density core in a circular velocity analysis (Valenzuela et al. 2007). Pressure support in the rotating gas of low mass galaxies could mask the underlying dark matter distribution, but the importance of this effect remains uncertain (Dalcanton & Stilp 2010).

The aim of this work is to investigate whether cusps in (LSB) dark matter haloes could still be mistaken for cores if high-resolution two-dimensional velocity fields data are available (as e.g. in Kuzio de Naray et al. 2009). In order to do so, we use self-consistent high-resolution simulations of

* Current Address: Department of Physics, Royal Military College of Canada, P.O. Box 17000, Station Forces, Kingston, ON, K7K 7B4, Canada

† E-mail: kuzio@rmc.ca

‡ E-mail: tobias.kaufmann@phys.ethz.ch

(LSB) galaxy formation and “observe” the simulated galaxies using the DensePak Integral Field Unit. We compare the mock velocity fields for different signatures from cuspy and cored haloes, spherical and triaxial potentials, and the effect of supernovae feedback. We also determine how well the underlying dark matter halo potential can be recovered.

The outline of the paper is as follows. In Section 2, we present the modeling of our initial conditions, the code used for the time evolution and the halo parameters derived from the simulations. In Section 3, we discuss the process of observing the simulations. The mock velocity fields and rotation curves are presented in Section 4. In Section 5, we present the halo fits to the mock data. A discussion and summary are presented in Section 6.

2 SMOOTHED PARTICLE HYDRODYNAMIC SIMULATIONS

We perform non-cosmological high-resolution N-Body/SPH (smoothed particle hydrodynamics) simulations of disc galaxy formation by cooling a rotating gaseous mass distribution inside equilibrium cuspy spherical, cored spherical, and cuspy triaxial dark matter haloes similar to what is described in Kaufmann et al. (2007a). The halo parameters were chosen to form extended discs with masses of a few $\times 10^8 M_\odot$ without bars or massive bulges in a dark halo with $c_{200} \sim 8.5$, as is common in low mass galaxies (K06). While these simulations are not modeling the full complexity of disc formation (e.g. mergers are missing) the dynamics of a disc dominated by a dark halo (i.e. the late phase of disc formation) is followed self-consistently and with high numerical resolution.

2.1 Initial conditions

Our initial conditions for the spherical runs comprise an isolated equilibrium cuspy or cored galaxy-sized halo with an embedded spinning gaseous mass distribution initially in hydrostatic equilibrium. The halo models are built as in Kazantzidis et al. (2004), and hence they include a self-consistent description of the velocity distribution function. Those models with virial mass of $M_{200} = 1.3 \times 10^{11} M_\odot$ were constructed using the $\alpha\beta\gamma$ models as described in Zemp et al. (2008). Cuspy haloes were modeled using the NFW form (1,3,1 for α,β,γ) and $c_{200} = 8.5$ following Macciò et al. (2008). For cored haloes, the parameters were set to 0.8,3,0 and $c_{200} = 24$. This choice produced an initial core with a radius of ~ 2 kpc, similar to what has been found in observational work (K06).

We initialise a fraction of the virial halo mass, $f_b = 0.01$, as a hot baryonic component with the same radial distribution as the dark matter. The initial temperature structure of the gaseous halo is calculated by solving the equation for the hydrostatic balance of an ideal gas inside a dark matter halo. The gas halo is spun with a gas spin parameter of $\lambda_g = 0.06$, and the dark matter particles are initialised with no net angular momentum (see Kaufmann et al. (2007a) for details). We note that the baryon fraction is much lower than the universal baryon fraction of ~ 0.17 , though this is not unexpected in low mass galaxies (McGaugh et al. 2010).

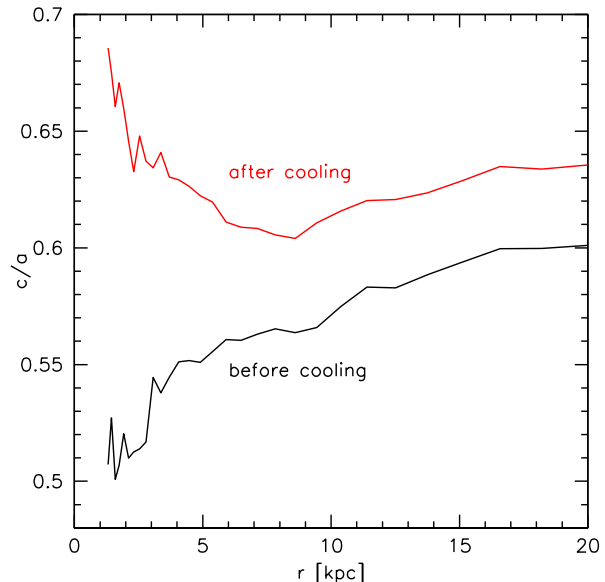


Figure 1. The ratio between the short and long axes of the dark matter density distribution of the triaxial halo before cooling (black line) and at the time of the disc analysis (red line).

This choice of f_b forms discs with masses of a few $\times 10^8 M_\odot$ in our models.

The models use 2.5×10^6 dark matter and 2×10^5 gas particles (mass of a dark particle $\sim 7 \times 10^4 M_\odot$) and have a spatial resolution (softening length) of 100 pc.

To construct an equilibrium triaxial halo in which the gas acquires its angular momentum through an equal mass merger (see Moore et al. 2004; Kaufmann et al. 2007a), we start with two spherical, non-rotating NFW haloes each with half of the mass and particles of the fiducial model considered previously. The two haloes are placed at a separation of twice their virial radius. One of them is given a transverse velocity of 27 km s^{-1} , and the haloes are allowed to merge. This net velocity (determined using a trial-and-error procedure) results in a final gas distribution that has a similar spin parameter to that used in the spherical models. The triaxial halo resulting after the merger is first evolved for 15 Gyr with an adiabatic equation of state for the gas. The inner part of the dark halo is significantly triaxial, $c/a \approx 0.6$ (and $b/a \approx 0.7$) and the subsequent formation of the disc due to cooling modifies the shape of the dark matter only weakly (see Figure 1 and also Kazantzidis et al. (2010)).

2.2 Time evolution and derived halo parameters

All of the systems were then evolved for ~ 4.5 Gyr using the parallel TreeSPH code GASOLINE (Wadsley 2004), which is an extension of the pure N-Body gravity code PKDGRAV developed by Stadel (2001). The code implements Compton and radiative cooling, as well as the star formation and “blastwave feedback” prescriptions detailed in Katz et al. (1996) and Stinson et al. (2006). In order for star particles to form, the gas temperature must be $< 30,000 \text{ K}$, the local gas density must be $> 0.1 \text{ cm}^{-3}$ and other local gas particles must define a converging flow. Stars then

Table 1. Dark halo parameters derived from the simulations after the evolution with cooling

Name	R_{200} or r_{core}	c_{200} or ρ_{core}
Cuspy	104.8 kpc	8.4
Cuspy SN	104.3 kpc	8.3
Triaxial	102.9 kpc	8.8
Cored	1.5 kpc	$69 \times 10^{-3} M_{\odot} \text{ pc}^{-3}$

form according to the Schmidt law (Kennicutt 1998) using a Miller & Scalo (1979) initial mass function. The supernova (SN) feedback model creates turbulent motions in nearby gas particles that keep them from cooling and forming stars. Because of the lack of metal and molecular cooling, the efficiency of our cooling function drops rapidly below 10^4 K acting as a temperature floor similar to what has been used in Kaufmann et al. (2007b). Star formation is only switched on in the cuspy model using the feedback prescription¹; the other simulations are cooling-only runs.

At the time of the analysis, thin, extended baryonic discs resembling LSB galaxies have formed in the centre of the haloes. This redistribution of the baryonic matter due to cooling also affects the underlying dark matter distribution, see below. The discs do not show bars or massive bulges, have baryonic masses of $\sim 5 \times 10^8 M_{\odot}$, and star formation rates, $SFR \sim 0.33 M_{\odot} \text{ yr}^{-1}$, comparable to those observed in LSB galaxies (Wyder et al. 2009). The discs are dark matter-dominated with the baryonic mass reaching up to 30% of the total mass within the inner 0.5 kpc and far less beyond. The galaxies formed in the spherical simulations lie between the mean and the upper 2σ deviation of the (observational) Radius-Velocity relation presented in Dutton et al. (2007), while the galaxy formed in the triaxial simulation lies just above the upper 2σ deviation from the mean. These somewhat large radial scale-lengths are not unexpected as the spin parameter chosen in the initial conditions was above the mean. Additionally, it has been suggested by Macciò et al. (2007) that LSB galaxies reside in haloes with spins higher than average.

We derive halo parameters after the evolution with cooling directly from the simulations and list them in Table 1. Additionally, in Table 1 we establish our naming convention for the simulations. We refer to the spherical cuspy simulation without feedback as ‘Cuspy’; the spherical cuspy simulation with feedback is referred to as ‘Cuspy SN’. The triaxial cuspy simulation is referred to as ‘Triaxial’ and the spherical cored simulation is referred to as ‘Cored’. Motivated by the parameterisations used in observational works (e.g. de Blok 2010) we fit an NFW profile (Navarro et al. 1996a) to the dark matter density curves derived from the cuspy simulations and a pseudoisothermal sphere profile (as in e.g. K06) to the cored simulation.

The initial and final halo shapes do not differ significantly, even in the simulation with feedback. In our simulations, massive dark matter haloes are in place at the beginning of the simulation and the low mass present in baryons

($f_{baryons} = 0.01$) is of little importance for the dynamics of the dark matter (specifically, the mass of blown-out baryons is too small to affect the dynamics of the dark halo). The only potential influence from the supernova feedback is a disturbance of the velocity field of the gas in the galactic disc. This is different than the cosmological simulations of Governato et al. (2010) (using the same feedback prescription but a higher minimal density for star formation) who find that cored dark matter haloes are created due to strong outflows from supernovae in dwarf galaxies. The outflows remove the central dark matter cusp at high redshift when the dark matter halo is less massive.

3 “OBSERVING” THE SIMULATIONS

Each galaxy+halo simulation is “observed” under a variety of instrumental configurations and physical properties designed to represent a range of mock data quality from ideal to realistic. We test three distances, 15 Mpc, 30 Mpc, and 45 Mpc, corresponding to spatial resolutions of $\sim 0.07 \text{ kpc}''$, $0.15 \text{ kpc}''$, and $0.22 \text{ kpc}''$, respectively. The choice of these spatial resolutions was motivated by the spatial resolution obtained for the LSB galaxies observed in K06 and K08, as well as a requirement that a $3''$ IFU fiber provide sub-kiloparsec resolution. We test three galaxy inclinations, $i = 30^\circ$, 50° , 65° , the range again being motivated by the data presented in K06 and K08. There is an inherent trade-off between inclination and obtaining a well-sampled velocity field, and most observational studies target galaxies having inclinations within, or very close to, this range (e.g. Spano et al. 2008; Blais-Ouellette et al. 2004). Not all lines of sight in nonaxisymmetric systems are equivalent (Kuzio de Naray et al. 2009), so we also rotate the galaxy+halo system by a random angle in the plane of the disc. For consistency, we do this for the spherical simulations in addition to the triaxial simulation.

DensePak, an integral field spectrograph on the 3.5-m WIYN telescope at the Kitt Peak National Observatory (KPNO), is used to “observe” each simulated galaxy. DensePak is a $43'' \times 28''$ fixed array of $3''$ fibers with $3.84''$ separations. We model the 85 working, and five missing or broken, fibers in the main bundle. We test three configurations of DensePak fiber alignment (see Figure 2). In the Ideal case, 11 pointings of the IFU array provide maximum spatial coverage across the galaxy. In the Realistic 1 and Realistic 2 cases, there are 5 pointings of the IFU array. In the Realistic 1 case, the IFU fibers cover the central region of the mock galaxy. The IFU fibers are along the mock galaxy major axis in the Realistic 2 configuration. The velocity recorded for each fiber is the average of all the line-of-sight velocities of the gas particles falling within the fiber. In the Ideal case, all 935 IFU fibers provide a velocity measurement. To simulate the sparse $H\alpha$ emission observed in some real galaxies, $\sim 40\%$ of the fibers in the Realistic 1 and 2 cases are randomly turned off so that no velocity measurement is obtained. Finally, we ensure that the fiber-to-fiber velocity variation is $6\text{--}10 \text{ km s}^{-1}$, consistent with the velocity dispersion measured in the K06 galaxies.

Mock velocity fields are obtained using all three IFU fiber configurations at the high and medium spatial resolutions. Only the Ideal and Realistic 2 configurations are used

¹ Heating by a uniform UV background from QSO following Haardt & Madau (1996) has also been used.

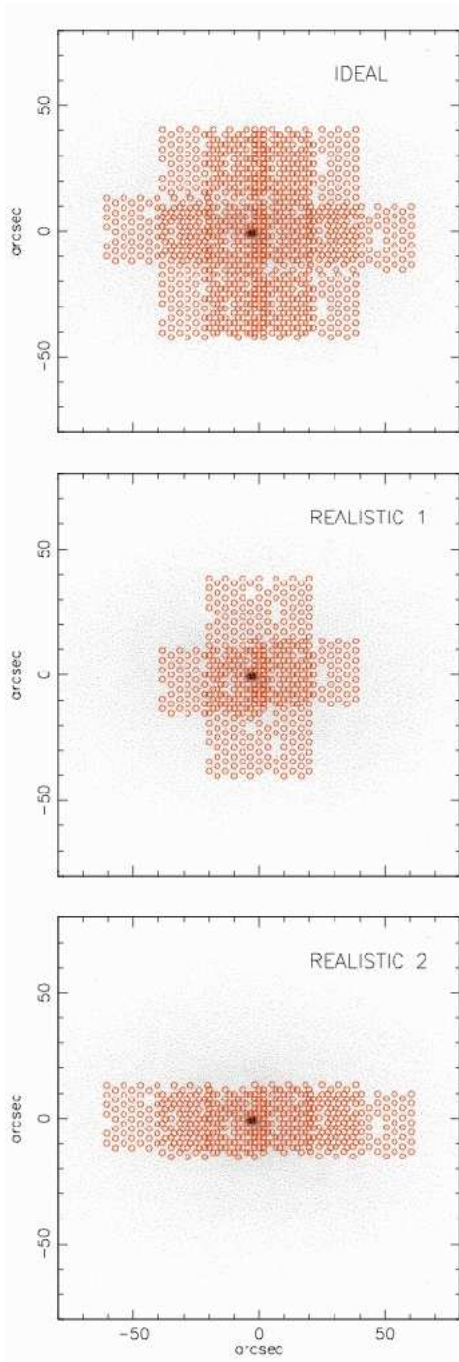


Figure 2. Configurations of the IFU fibers (red circles) shown on the galaxy (grey points). *Top:* There is maximum spatial coverage across the galaxy in the Ideal configuration and all fibers provide a velocity measurement. *Middle:* In the Realistic 1 configuration, the reduced number of fibers cover the central part of the galaxy. Additionally, $\sim 40\%$ of the fibers shown are randomly turned off so that not all fibers provide a velocity measurement. *Bottom:* The fibers in the Realistic 2 configuration are along the galaxy major axis. As in the Realistic 1 configuration, not all fibers provide a velocity measurement.

at low spatial resolution because of the reduced angular size of the galaxy. The three galaxy inclinations are tested at each spatial resolution and IFU fiber configuration. For each galaxy+halo simulation, we obtain five mock velocity fields at each combination of galaxy parameters and IFU configurations. Our final data set includes 120 mock velocity fields per galaxy+halo simulation, for a total of 480 mock velocity fields.

4 MOCK DATA

In this section, we present examples of the mock velocity fields and derived rotation curves for each of the four galaxy+halo simulations.

4.1 Mock velocity fields

In Figures 3-6, we show four representative examples of the mock velocity fields obtained for each simulation, covering the range of spatial resolutions, inclinations, and IFU configurations. The velocity fields in the upper left and lower right are examples of the data obtained using the Ideal configuration while the upper right shows an example of the Realistic 1 configuration and the lower left an example of the Realistic 2 configuration. Figure 3 contains mock velocity fields for the triaxial simulation. Mock velocity fields for the spherical cuspy simulation are in Figure 4, those including feedback are in Figure 5. Figure 6 contains mock velocity fields for the cored simulation.

In general, the mock velocity fields of the triaxial simulation (Figure 3) are characterised by misaligned kinematic and photometric major axes, and non-perpendicular kinematic major and minor axes (see Figure 7). Most noticeably, the minor axis is often twisted. Though no physical bar is present in the simulation, these are features commonly observed in the velocity fields of barred galaxies (e.g. Bosma 1981; Hernandez et al. 2005). Bar-like dynamical signatures (without an obvious bar) are also expected based on simulation work for subdominant discs in triaxial halos (Kazantzidis et al. 2010). The orientation of the twist varies in the different mock velocity fields depending on the angle between the observer’s line-of-sight and the potential.

The kinematic and photometric major axes are aligned in the mock velocity fields of the spherical cuspy simulations (Figures 4 and 5), and the major and minor kinematic axes are perpendicular. The isovelocity contours are noticeably pinched at the centre of the velocity field. There is very little difference between the mock velocity fields of the simulations with feedback and those without. The deposition of energy due to the supernovae did not affect the average velocity field in the cold gas heavily, thus it is still tracing the underlying (dark matter) potential quite closely.

The mock velocity fields of the cored simulation (Figure 6) are characterised by parallel isovelocity contours at the centre. The kinematic major and minor axes are perpendicular, and the kinematic and photometric major axes are aligned. The central regions of these velocity fields are very similar to those of dwarf and LSB galaxies (e.g. Gentile et al. 2005; K06).

We find through visual inspection of the 480 mock velocity fields, that depending on the underlying halo type, the

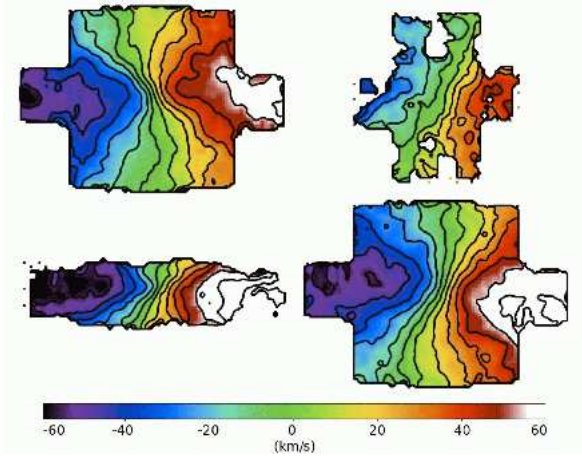


Figure 3. Sample mock velocity fields of the triaxial cuspy simulations; isovelocity contours are at 10 km s^{-1} intervals. The velocity fields in the upper left and lower right are examples of the Ideal configuration; the upper right and lower left are examples of the Realistic 1 and Realistic 2 configurations, respectively. The kinematic and photometric major axes are not aligned, the kinematic major and minor axes are not perpendicular, and the minor axis is often twisted.

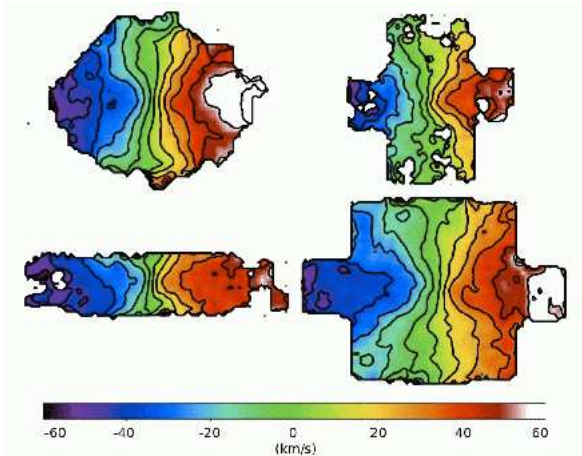


Figure 4. Sample mock velocity fields of the spherical cuspy simulations; isovelocity contours are at 10 km s^{-1} intervals. The layout is the same as Figure 3. The kinematic and photometric major axes are aligned, the kinematic major and minor axes are perpendicular, and the isovelocity contours are pinched at the centre of the velocity field.

mock velocity fields look distinctly different. We capture the distinguishing features discussed above in the illustration in Figure 8. We can quantify these differences by comparing velocities measured along slits placed parallel to the minor axis. In Figure 9, we plot the average of the measured velocities in a $3'' \times 28''$ slit (the width of a DensePak fiber and the width of the DensePak array, respectively) parallel to and offset from the minor axis by $\pm 0.5 \text{ kpc}$. The velocity is roughly constant as a function of position along the slit in the cored mock velocity fields, consistent with the generally parallel isovelocity contours. The pinch observed in the spherical cuspy mock velocity fields translates to a symmetric $\sim 8 \text{ km s}^{-1}$ rise in velocity along the slit as the major

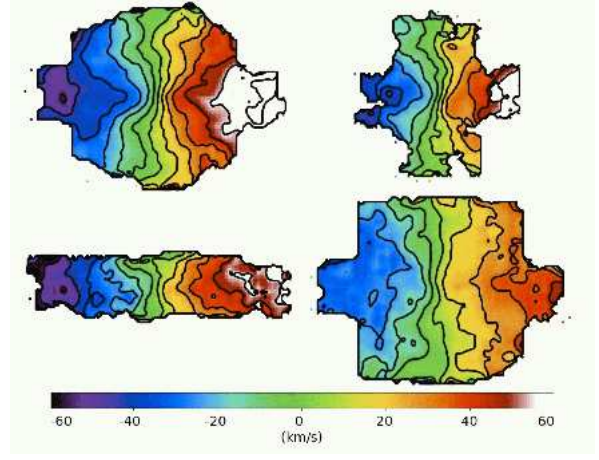


Figure 5. Sample mock velocity fields of the spherical cuspy SN simulations; isovelocity contours are at 10 km s^{-1} intervals. The layout is the same as Figure 3. The kinematic and photometric major axes are aligned, the kinematic major and minor axes are perpendicular, and the isovelocity contours are pinched at the centre of the velocity field.

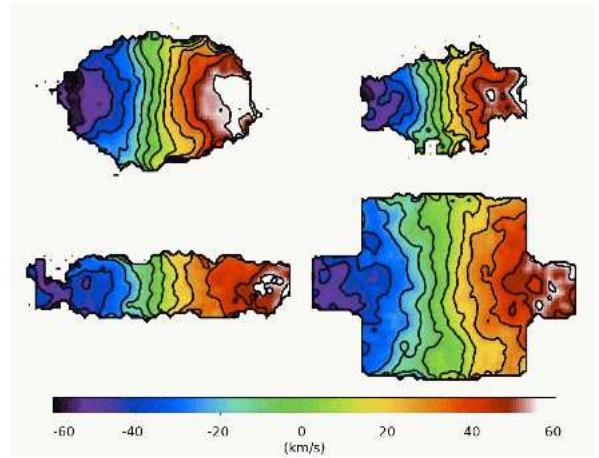


Figure 6. Sample mock velocity fields of the spherical cored simulations; isovelocity contours are at 10 km s^{-1} intervals. The layout is the same as Figure 3. The kinematic and photometric major axes are aligned, the kinematic major and minor axes are perpendicular, and the isovelocity contours are parallel at the centre of the velocity field.

axis ($r = 0$) is approached. When slits are placed parallel to the photometric minor axis in the triaxial mock velocity fields, there is an asymmetric (around $r = 0$) overall change in velocity of $\sim 16 \text{ km s}^{-1}$ along the slit. This behavior is unique to the triaxial case; velocities measured along slits placed at an angle to the minor axis in the spherical cuspy and cored cases show a steady change (constant increase or decrease) in velocity along the entire length of the slit. It is important to note that the differences in the central regions of the mock velocity fields are equally detectable at all three spatial resolutions. That the underlying halo type produces a unique and measurable signature in the observed velocity field is an important result. It means that the halo profile can be probed in a model-independent way.

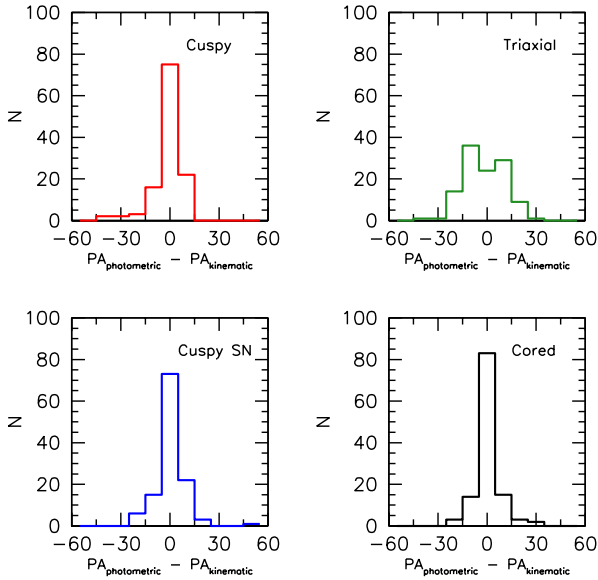


Figure 7. Difference in degrees between the photometric and kinematic major axes as measured at a radius of $19.5''$, approximately half the length of a single DensePak pointing. The axes are aligned in the majority of the spherical cuspy (with and without feedback) and cored mock velocity fields; the axes are frequently misaligned in the triaxial mock velocity fields.

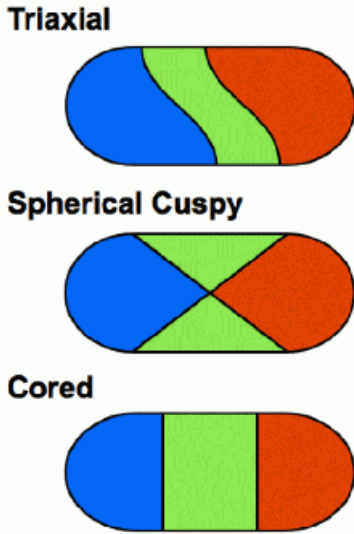


Figure 8. Schematic representations of the distinguishing features of the triaxial cuspy, spherical cuspy, and spherical cored mock velocity fields.

4.2 Application to LSB galaxy data

We apply the slit method described in Section 4.1 to the DensePak velocity fields of the LSB galaxies presented in K06 and K08 to see how well it compares to the results obtained for the galaxies by fitting halo models to the rotation curves. We plot the results for 5 of the galaxies in Figure 10. K06 and K08 find the cuspy NFW halo to provide a

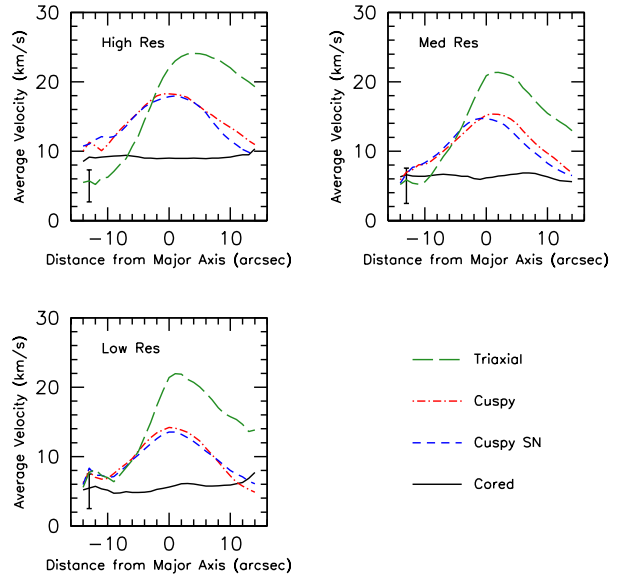


Figure 9. Average velocity measured along slits parallel to, and offset from, the minor axis of the mock velocity fields. A typical errorbar is shown in the lower left corner.

better fit to the rotation curve of NGC 4395 than the cored isothermal halo; they also note a misalignment of the minor axis. In Figure 10, the change in velocity along the slit in NGC 4395 displays the same shape as those along the triaxial slits in Figure 9. There is an asymmetric (around $r = 0$) overall change in velocity of $\sim 18 \text{ km s}^{-1}$ along the slit. Within the errors, the velocities are roughly constant along the slits for UGC 4325, DDO 64, and F583-1. A constant velocity is expected for cored haloes, and these three galaxies are found to be best-described by cored isothermal haloes in K06 and K08. K08 find the rotation curve of NGC 7137 to be equally fit by cored and cuspy haloes. In Figure 10, the velocities along the slit in NGC 7137 display a close to symmetric (around $r = 0$) $\sim 6 \text{ km s}^{-1}$ change in velocity. This behavior is similar to the change in the velocity seen along the spherical cuspy slits in Figure 9. We find that the slit method can provide a measure of the underlying halo in real galaxy data that is in agreement with results based on the traditional method of rotation curve fitting.

4.3 Mock rotation curves

The NEMO (Teuben 1995) program ROTCUR (Begeman 1989) is used to derive a rotation curve from each mock velocity field. ROTCUR treats the observed velocity field as an ensemble of tilted rings and fits for the centre, systemic velocity, inclination, position angle, and rotation velocity in each ring. We allow the position angle to change with radius, but we do not make any explicit attempts to model the obvious non-circular motions when fitting the triaxial velocity fields. For an extensive explanation of ROTCUR and its application to the DensePak velocity fields, the reader is referred to K06 and K08. We also calculate the rotation curve directly from each of the four galaxy+halo simulations assuming $V^2 = GM/r$.

In Figure 11, we compare the rotation curves extracted

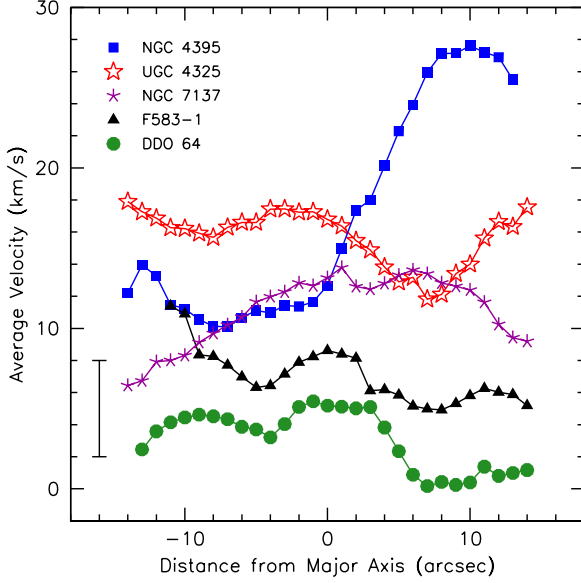


Figure 10. Average velocity measured along slits parallel to, and offset from, the minor axis of galaxies from K06 and K08. A typical errorbar is shown in the lower left corner.

from each mock velocity field to the rotation curves derived from the simulations. Overall, we find the mock rotation curves to trace the simulation rotation curves well. The rotation curves extracted from the triaxial velocity fields show a large spread in velocity at all radii, not surprising given the dependence on the observer’s line-of-sight with respect to the orientation of the potential. There is much less variation in the mock rotation curves extracted from the spherical cuspy and cored velocity fields. In addition, the comparisons of the average mock rotation curves to the rotation curves derived directly from the simulations are practically indistinguishable. In all three cases, the average mock rotation curve is only $\sim 3 \text{ km s}^{-1}$ below the simulation rotation curve at small radii ($r \lesssim 1 \text{ kpc}$), is equal to the simulation at intermediate radii, and displays a trend toward slightly higher average velocities at large radii.

5 HALO FITS

Following the convention of observational studies, we fit each mock rotation curve with both the cuspy NFW halo and the cored pseudoisothermal halo. We fit the data under the assumption of negligible baryonic mass. The NFW rotation curve is given by

$$V(R) = V_{200} \sqrt{\frac{\ln(1+cx) - cx/(1+cx)}{x[\ln(1+c) - c/(1+c)]}}, \quad (1)$$

with $x = R/R_{200}$. Here R_{200} is the radius at which the density contrast exceeds 200, V_{200} is the circular velocity at R_{200} , and the concentration parameter $c = R_{200}/R_s$, where R_s is the characteristic radius of the halo (Navarro et al. 1996a, 1997). The rotation curve of the pseudoisothermal halo is given by

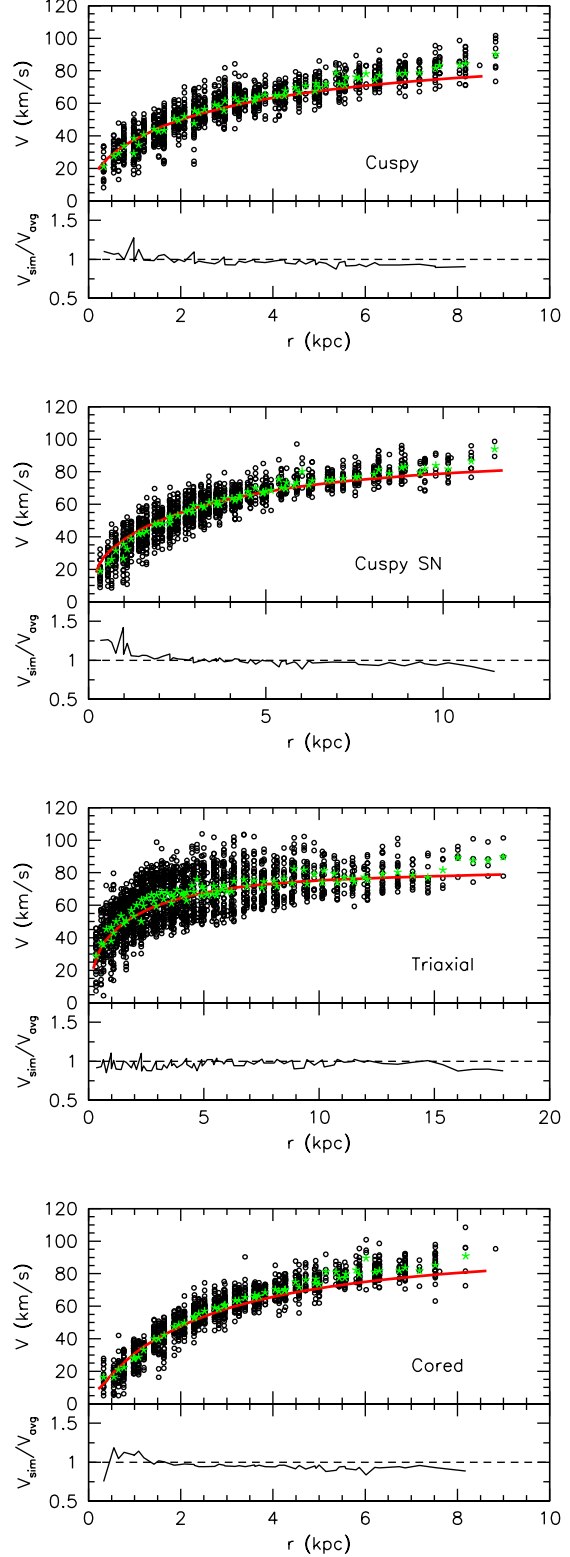


Figure 11. Comparison of the recovered mock rotation curves (black open circles) to the rotation curve derived from the simulation (red line) using $V^2 = GM/r$. The green stars are the average mock rotation curve. The bottom panels plot the ratio of the simulation rotation curve to the average mock rotation curve.

$$V(R) = \sqrt{4\pi G \rho_0 R_C^2 \left[1 - \frac{R_C}{R} \arctan\left(\frac{R}{R_C}\right) \right]}, \quad (2)$$

where ρ_0 is the central density of the halo and R_C is the core radius of the halo.

In Figure 12, we show the distribution of the recovered halo parameters (c , R_{200} ; ρ_0 , R_c) from the fits to the mock data (In the following, R_{200} , ρ_0 and R_c are given in units of kpc, $10^{-3} M_\odot \text{ pc}^{-3}$ and kpc, respectively). We find that the parameter values obtained from the fits to the mock rotation curves are in agreement with those derived directly from the simulations (Table 1). The parameters of the best-fitting NFW halo to the spherical cuspy data are $c = 9.4 \pm 1.8$ and $R_{200} = 107 \pm 10$; for the spherical cuspy with feedback data, the values are $c = 8.5 \pm 3.0$ and $R_{200} = 113 \pm 20$. There is more variation in the halo fits to the triaxial cuspy data. The best-fitting halo parameters are $c = 11.0 \pm 4.5$ and $R_{200} = 87 \pm 10$. The parameters of the best-fitting isothermal halo to the spherical cored data are $R_c = 2.0 \pm 0.5$ and $\rho_0 = 50 \pm 5$.

Fitting a pseudoisothermal sphere to the cuspy data results in dense, small cores ($\rho_0 \gtrsim 80$; $R_c \lesssim 1.0$); similarly, when fitting cuspy haloes to the cored data, the data want $c < 1.0$ and high R_{200} . This is not surprising since a profile with a tiny core and high central density resembles a cuspy profile and only with a very low concentration can one stretch an NFW curve to fit the rotation curve of a cored halo, see de Blok (2010). However, given the information from the velocity fields, one can easily break this ambiguity and identify the underlying halo shape even before fitting a profile to it. Additionally, the mass-concentration relation of CDM (Macciò et al. 2008) would predict $c < 1.0$ halos to have rotation velocities many times higher than the galaxy itself.

In Figure 13 are representative examples of residual mock velocity fields showing the differences between the mock data and the best-fitting cuspy and cored halo models. For the cored mock velocity fields, we display the residuals obtained when subtracting the best-fitting spherical cuspy halo model; the residuals obtained when comparing the cored data to the best-fitting spherical cuspy with feedback halo model are comparable. The residuals are small, typically less than $\sim 4 \text{ km s}^{-1}$, when cusps are fit to cusps and cores are fit to cores. When a core is fit to the cuspy data or a cusp is fit to the cored data, the residuals can become quite large. Residuals as high as $\sim 15 \text{ km s}^{-1}$ and $\sim 30 \text{ km s}^{-1}$ are obtained when cores are fit to the spherical and triaxial cuspy data, respectively; residuals on the order of 15 km s^{-1} are obtained when cusps are fit to the cored data.

We also calculate the inner slope of the mass density profile by converting the mock rotation curves using

$$\rho(R) = \frac{1}{4\pi G} \left[2 \frac{V}{R} \frac{\partial V}{\partial R} + \left(\frac{V}{R} \right)^2 \right], \quad (3)$$

where G is the gravitational constant and V is the observed rotation velocity at radius R (de Blok et al. 2001).

In Figure 14, we show the distribution of the asymptotic inner slope of the dark matter density profiles derived from the mock rotation curve data. The gray shaded regions indicate the inner slopes derived directly from the dark matter densities of the simulations. We find the cuspy halos to generally have inner slopes of -1 or steeper and the inner

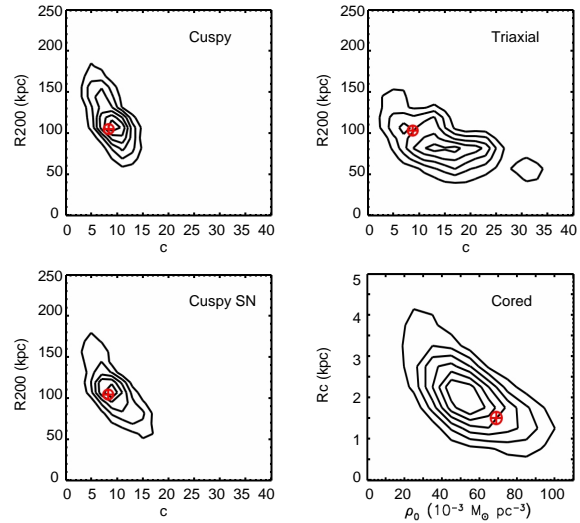


Figure 12. Recovered halo parameters from the mock velocity fields and rotation curves. The contours represent the distribution of parameters found with the mock observations and the red crossed circles indicate the values of the parameters derived directly from the simulations.

slope of the cored halo to be more shallow, around a value of ~ -0.4 . The inner slopes derived directly from the simulations are -1.3 , -1.4 , -1.4 , and -0.3 for the spherical cuspy, spherical cuspy with feedback, triaxial cuspy, and spherical cored halos, respectively. The corresponding inner slopes determined from the mock data are -1.0 ± 0.7 , -1.0 ± 0.8 , -1.4 ± 0.7 , and -0.5 ± 0.4 .

6 DISCUSSION AND CONCLUSIONS

We have presented mock velocity fields, rotation curves, and halo fits for simulated LSB galaxies formed in spherical and triaxial cuspy dark matter haloes and spherical cored dark matter haloes. The mock velocity fields span a range of data quality representing ideal to realistic observations. The main findings of this work are:

- The underlying halo type produces a unique signature in the velocity field. This can be used to constrain the shape of the dark matter profile (spherical or triaxial cuspy, or spherical cored) without fitting an analytic density profile to it.
- Cored and cuspy haloes can also be distinguished clearly by deriving their asymptotic inner slopes from the rotation curve data.
- Given at least one of the above information one can then successfully recover the underlying halo parameters from the rotation curve using the appropriate analytic form for the density profile (NFW or pseudoisothermal sphere).

This means that if an LSB galaxy were in a cuspy halo, the cusp would be observable in the data. Given these results, we find it difficult to mistake cuspy haloes, spherical or triaxial, for cored haloes. The observed cores in dark matter-dominated galaxies are true discrepancies from the predictions of (dark matter-only) Λ CDM simulations. Systematic effects, non-circular motions, and halo triaxiality cannot explain the observed differences.

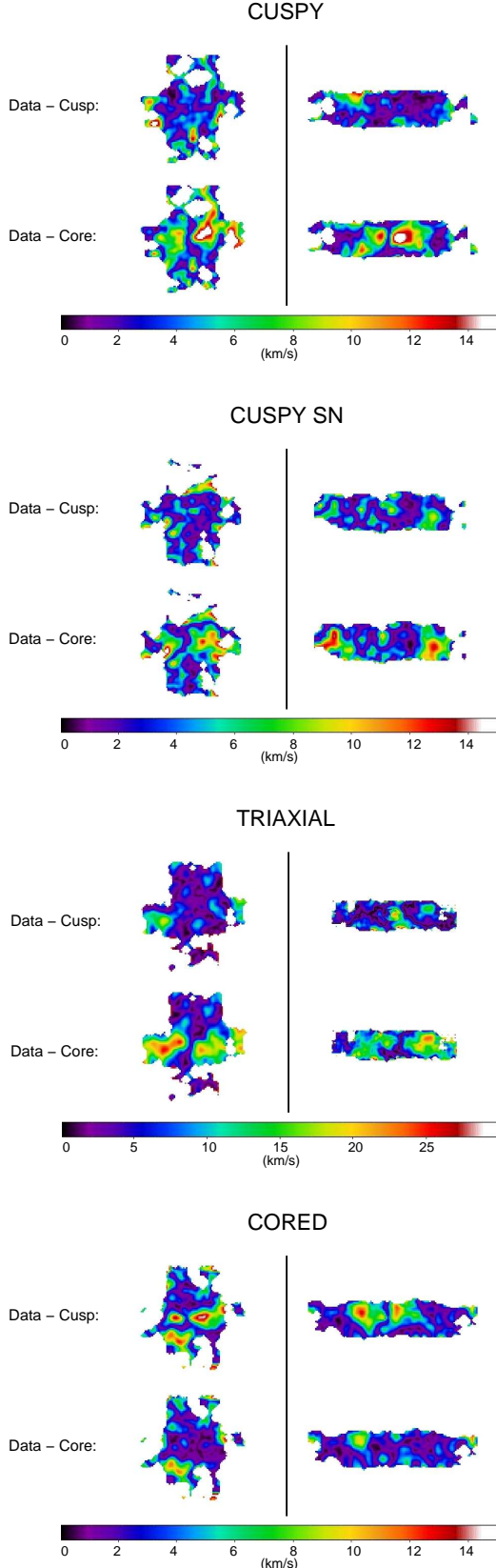


Figure 13. Sample residual velocity fields after subtracting the best-fitting cuspy and cored halo models from two different observed mock velocity fields (Realistic 1 case on the left, Realistic 2 case on the right.)

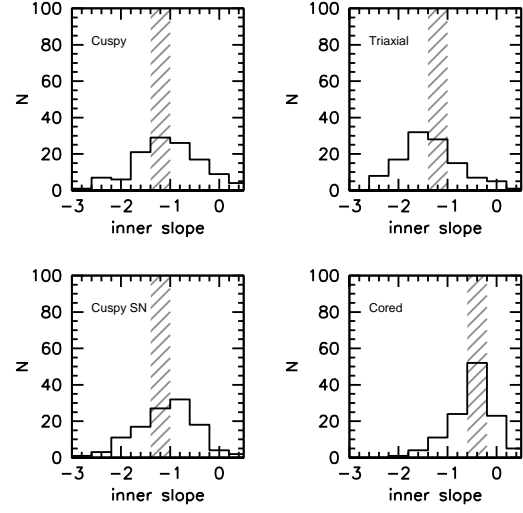


Figure 14. Distribution of the asymptotic inner slope of the dark matter density profiles derived from the mock rotation curve data. The gray shaded regions indicate the inner slope derived directly from the dark matter densities of the simulations.

Baryonic processes more effective than those we have modeled or entirely different dark matter models may be necessary to explain the observed cores. Feedback from star formation could transform the initial cusps into cores. If LSB galaxies form with a massive dark matter halo already in place and with the same low baryon fraction that we observe today, then feedback from star formation of the type we have modeled would not be enough to change a cusp into a core. In this scenario, the dark matter halos in which LSB galaxies reside cannot be cuspy CDM halos. If, however, feedback processes from star formation can affect dark matter haloes during the early stages of their formation, it is possible that cusps can be transformed into cores. This has been demonstrated by Governato et al. (2010) (see also Oh et al. (2010)) using a set of fully cosmological simulations of dwarf galaxy formation ($M_{vir} \sim 3 \times 10^{10} M_{\odot}$) where strong outflows from supernovae remove low-angular-momentum gas and decrease the dark matter density to less than half in the central part (see also Navarro et al. 1996b; Read & Gilmore 2005; Mashchenko et al. 2008). The question in this scenario then becomes one of detecting the blown-out baryons. It also remains to be seen if this kind of mechanism can act efficiently on higher mass scales, given the deeper potential wells.

Alternatively, the observed cores may need to be addressed by a different dark matter model/particle that naturally produces cored haloes. Recent results, however, have found that self-interactions and warm dark matter particle properties cannot be responsible for the cores observed in dark matter-dominated galaxies (e.g. Kuzio de Naray et al. 2010; Villaescusa-Navarro & Dalal 2010).

ACKNOWLEDGMENTS

The work of R. K. D. was supported by NSF Astronomy & Astrophysics Postdoctoral Fellowship grant AST 0702496. T. K. acknowledges financial support from the Swiss Na-

tional Science Foundation (SNF). It is a pleasure to thank James Wadsley, Joachim Stadel and Tom Quinn for making GASOLINE available to us. We acknowledge useful and stimulating discussions with James Bullock, Fabio Governato and Stacy McGaugh.

REFERENCES

- Bailin J., Simon J. D., Bolatto A. D., Gibson B. K., Power C., 2007, *ApJ*, 667, 191
- Begeman K., 1989, *A&A*, 223, 47
- Blais-Ouellette S., Amram P., Carignan C., Swaters R., 2004, *A&A*, 420, 147
- Bosma A., 1981, *AJ*, 86, 1825
- de Blok W. J. G., Bosma A., 2002, *A&A*, 385, 816
- de Blok W. J. G., 2010, *Advances in Astronomy*, 2010
- de Blok W. J. G., McGaugh S. S., Bosma A., Rubin V.C., 2001, *ApJ*, 552, 23
- de Blok W. J. G., Walter F., Brinks E., Trachternach C., Oh S. H., Kennicutt R.C., 2008, *AJ*, 136, 2648
- Dalcanton J. J., Stilp A. M. 2010, *ApJ*, 721, 547
- Dutton A. A., van den Bosch F. C., Dekel A., Courteau S. 2007, *ApJ*, 654, 27
- Gentile G., Burkert A., Salucci P., Klein U., Walter F., 2005, *ApJ*, 634, L145
- Governato F., et al., 2010, *Nature*, 463, 203
- Graham A. W., Merritt D., Moore B., Diemand J., Terzić B., 2006, *AJ*, 132, 2701
- Haardt F., & Madau P. 1996, *ApJ*, 461, 20
- Hayashi E., Navarro J. F., Springel V., 2007, *MNRAS*, 377, 50
- Hernandez O., Carignan C., Amram P., Chemin L., Daigle O., 2005, *MNRAS*, 360, 1201
- Katz N., Weinberg D. H., Hernquist L., 1996, *ApJS*, 105, 19
- Kaufmann T., Mayer L., Wadsley J., Stadel J., Moore B., 2007a, *MNRAS*, 375, 53
- Kaufmann T., Wheeler C., Bullock J. S., 2007b, *MNRAS*, 382, 1187
- Kazantzidis S., Abadi M. G., Navarro J. F. 2010, *ApJ*, 720, L62
- Kazantzidis S., Magorrian J., Moore B., 2004, *ApJ*, 601, 37
- Kennicutt R. C., Jr., 1998, *ApJ*, 498, 541
- Kuzio de Naray R., Martinez G. D., Bullock J. S., Kaplinghat M., 2010, *ApJ*, 710, L161
- Kuzio de Naray R., McGaugh S. S., de Blok W. J. G., 2008, *ApJ*, 676, 920 (K08)
- Kuzio de Naray R., McGaugh S. S., de Blok W. J. G., Bosma A., 2006, *ApJS*, 165, 461 (K06)
- Kuzio de Naray R., McGaugh S. S., Mihos J. C., 2009, *ApJ*, 692, 1321
- Macciò A. V., Dutton A. A., van den Bosch F. C., 2008, *MNRAS*, 391, 1940
- Macciò A. V., Dutton A. A., van den Bosch F. C., Moore B., Potter D., Stadel J. 2007, *MNRAS*, 378, 55
- Mashchenko S., Wadsley J., Couchman H. M. P., 2008, *Science*, 319, 174
- McGaugh S. S., Schombert J. M., de Blok W. J. G., Zargursky M. J., 2010, *ApJ*, 708, L14
- Miller G. E., Scalo J. M. 1979, *ApJS*, 41, 513
- Moore B., Quinn T., Governato F., Stadel J., Lake G., 1999, *MNRAS*, 310, 1147
- Moore B., Kazantzidis S., Diemand J., Stadel J., 2004, *MNRAS*, 354, 522
- Navarro J. F., Frenk C. S., White S. D. M., 1996a, *ApJ*, 462, 563
- Navarro J. F., Eke V. R., Frenk C. S., 1996b, *MNRAS*, 283, L72
- Navarro J. F., Frenk C. S., White S. D. M., 1997, *ApJ*, 490, 493
- Navarro J. F. et al. 2010, *MNRAS*, 402, 21
- Oh S.-H., Brook C., Governato F., Brinks E., Mayer L., de Blok W. J. G., Brooks A., Walter F. 2010, *arXiv:1011.2777*
- Read J. I., Gilmore G., 2005, *MNRAS*, 356, 107
- Spano M., Marcelin M., Amram P., Carignan C., Epinat B., Hernandez O., 2008, *MNRAS*, 383, 297
- Stadel J., 2001, PhD Thesis, U. Washington
- Stadel J., Potter D., Moore B., Diemand J., Madau P., Zemp M., Kuhlen M., Quilis V., 2009, *MNRAS*, 398, L21
- Stinson G., Seth A., Katz N., Wadsley J., Governato F., Quinn T., 2006, *MNRAS*, 373, 1074
- Teuben P.J. 1995, in *ASP Conf. Ser. 77, Astronomical Data Analysis Software and Systems IV*, ed. R. Shaw, H.E. Payne, & J.J.E. Hayes (San Francisco, CA: ASP), 398
- Valenzuela O., Rhee G., Klypin A., Governato F., Stinson G., Quinn T., Wadsley J. 2007, *ApJ*, 657, 773
- Villaescusa-Navarro F., Dalal N., 2010, *arXiv: 1010.3008*
- Wadsley J., Stadel J., Quinn T., 2004, *NewA*, 9, 137
- Wyder, T. K. et al., 2009, *ApJ*, 696, 1834
- Zemp M., Moore B., Stadel J., Carollo C. M., Madau P., 2008, *MNRAS*, 386, 1543